PHOTONICS Research

Whispering-gallery mode hexagonal micro-/nanocavity lasers [Invited]

Yue-De Yang,[1,2] Min Tang,[1,2] Fu-Li Wang,[1,2] Zhi-Xiong Xiao,[1,2] Jin-Long Xiao,[1,2] and Yong-Zhen Huang[1,2,*]

[1]State Key Laboratory of Integrated Optoelectronics, Institute of Semiconductors, Chinese Academy of Sciences, Beijing 100083, China
[2]Center of Materials Science and Optoelectronics Engineering, University of Chinese Academy of Sciences, Beijing 100049, China
*Corresponding author: yzhuang@semi.ac.cn

Received 31 January 2019; revised 14 March 2019; accepted 14 March 2019; posted 14 March 2019 (Doc. ID 359279); published 30 April 2019

Whispering-gallery-mode (WGM) hexagonal optical micro-/nanocavities can be utilized as high-quality (Q) resonators for realizing compact-size low-threshold lasers. In this paper, the progress in WGM hexagonal micro-/nanocavity lasers is reviewed comprehensively. High-Q WGMs in hexagonal cavities are divided into two kinds of resonances propagating along hexagonal and triangular periodic orbits, with distinct mode characteristics according to theoretical analyses and numerical simulations; however, WGMs in a wavelength-scale nanocavity cannot be well described by the ray model. Hexagonal micro-/nanocavity lasers can be constructed by both bottom-up and top-down processes, leading to a diversity of these lasers. The ZnO- or nitride-based semiconductor material generally has a wurtzite crystal structure and typically presents a natural hexagonal cross section. Bottom-up growth guarantees smooth surface faceting and hence reduces the scattering loss effectively. Laser emissions have been successfully demonstrated in hexagonal micro-/nanocavities synthesized with various materials and structures. Furthermore, slight deformation can be easily introduced and precisely controlled in top-down fabrication, which allows lasing-mode manipulation. WGM lasing with excellent single-transverse-mode property was realized in waveguide-coupled ideal and deformed hexagonal microcavity lasers.

https://doi.org/10.1364/PRJ.7.000594

1. INTRODUCTION

Optical microcavities, which enhance light–matter interaction by storing optical energy in small volumes (V) with low losses, have attracted considerable interest in both fundamental physics studies and practical device applications [1]. To achieve a high quality (Q) factor and a small mode volume simultaneously, the mode light should be confined inside a microcavity with near-unity reflectivity; this can be realized by the photonic forbidden band in vertical-cavity surface-emitting lasers and photonic crystal microcavities, or by total internal reflection (TIR) in whispering-gallery-mode (WGM) optical microcavities. Since photonic integration has become an important research topic nowadays, WGM optical microcavities with monolithic integration capability and low processing complexity have attracted significant attention [2–8]. The idea of WGMs came from the observation of an acoustical phenomenon in whispering galleries, and was later extended to electromagnetic waves [9]. By trapping light with continuous TIR at the cavity boundary, WGM microcavities can support optical modes with a large value of Q/V [7]. As the most representative cavity shapes, WGM microcavities with circularly rotational symmetries in different geometries have been widely studied for the demonstration of low-power-consumption compact photonic devices [10–37], e.g., ultralow-threshold microlasers.

Although circular WGM microcavities can have extremely high Q factors, one major shortcoming appears to be the isotropic emission along the cavity rim, which poses significant difficulty in the efficient collection of the output light from the circular microlasers. However, by properly designing the geometrical shape of the WGM microcavities to break the circularly rotational symmetry, directional output emission was realized for high-Q WGM asymmetric microcavities [38–48]. The mechanism of directional emission in these asymmetric microcavities was well explained by the chaotic ray dynamics. Furthermore, unidirectional emission was achieved in various WGM microcavities by carefully modifying the cavity geometries [49–59].

Besides circular WGM microcavities, regular polygonal microcavities supporting high-Q whispering-gallery-like modes (denoted as WGMs in the following text for short) have also been studied widely in the past decades for demonstrations of microlasers and add–drop optical filters [60–72]. Regular polygonal microcavities show distinct mode properties compared with circular microcavities when the side number is

not large [73]. For WGMs in equilateral-triangular and square microcavities with integrable internal dynamics, quasi-analytical solutions were obtained [68,70]. The dynamics is not integrable; instead, it is pseudo-integrable in regular polygonal microcavities with side number larger than 4, resulting in pseudo-integrable leakage loss for the WGMs [63,74]. The periodic orbits in general regular polygonal microcavities have been studied [75], and high-Q WGMs typically exist as superscar states along the periodic orbits with weak field distributions at the corners [76].

Interestingly, ZnO- or nitride-based semiconductor materials for ultraviolet (UV) laser diodes generally have a wurtzite crystal structure and typically present a natural hexagonal cross section [77–82]. Bottom-up synthesized structures allow smooth surface faceting and hence reduce the scattering loss effectively. WGM lasing has been successfully demonstrated in synthesized hexagonal micro-/nanocavity lasers [83–87]. On the other hand, slight deformation can be easily introduced and controlled in top-down fabrication processes, which allows lasing-mode manipulation and waveguide-coupled unidirectional emission [72,88–91]. WGM lasing was realized in organic single-crystalline and semiconductor hexagonal microcavity lasers. In this paper, the progress in WGM hexagonal micro-/nanocavity lasers is reviewed. This review is organized as follows. In Section 2, comprehensive studies are presented on the mode characteristics of hexagonal micro-/nanocavities, including analyses of ray dynamics and cavity symmetry, and numerical simulations of WGMs inside hexagonal cavities. In Section 3, experimental results of bottom-up grown hexagonal micro-/nanocavity lasers are presented. In Section 4, experimental results of top-down fabricated hexagonal microlasers are presented. Finally, the summary and outlook are given in Section 5.

2. OPTICAL MODES IN HEXAGONAL CAVITIES

A. Periodic Orbits in Hexagonal Microcavities

By assuming a given mode field distribution in the vertical direction, a practical three-dimensional (3D) hexagonal cavity can be simplified to a two-dimensional (2D) hexagon with an effective refractive index. The 2D model can give an accurate mode structure and predict high-Q WGMs efficiently, although it may give incorrect Q factors sometimes [70,92,93]. Figure 1(a) shows a simplified 2D hexagonal cavity with a side length of a in the x-y plane; here Ω_i and Ω_o are, respectively, the internal and external regions of the hexagon with refractive indices of n_i and n_o, and the center of the hexagon is placed at O. Both transverse-magnetic (TM) and transverse-electric (TE) polarized WGMs are considered in the analyses; here, TM (TE) WGMs are defined as modes with magnetic (electric) fields in the x-y plane and electric (magnetic) fields perpendicular to the plane. In the practical 3D case, the polarization of a mode is defined based on its dominant electromagnetic field components. Figure 1(b) shows the symmetry operators of the hexagonal microcavity.

Due to the non-integrable internal dynamics, there is a lack of analytical solution in a hexagonal microcavity. To give an intuitive description of WGMs, the semi-classical ray model

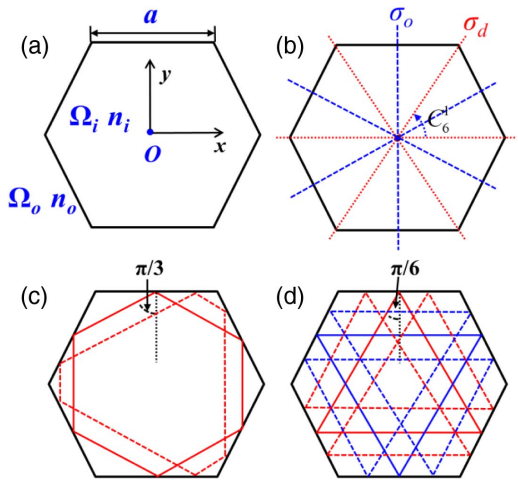

Fig. 1. (a) Schematic diagram and (b) symmetry operators of a 2D hexagonal microcavity. (c) The hexagonal periodic orbits and (d) the triangular periodic orbits in the hexagonal microcavity. The solid lines and dashed lines indicate, respectively, the ray trajectories connecting the midpoints of the sides and the other ray trajectories in the same orbit family with the same incident angles.

is introduced into a hexagonal microcavity with dimension much larger the optical wavelength.

Light can be confined along the hexagonal periodic orbits at the same incident angle of $\pi/3$ on the six sides as shown in Fig. 1(c). For a hexagonal microcavity with a refractive index ratio of $n_i/n_o > 2/\sqrt{3}$, these light rays can be totally reflected at the cavity sides. The solid line indicates the ray trajectory connecting the midpoints of adjacent sides, whereas the dashed line indicates one ray trajectory within the same orbit family with equal orbit length and incident angle. The WGMs corresponding to the hexagonal periodic orbits are the dominant modes in the hexagonal microcavity with a weak refractive index contrast, i.e., a small value of n_i/n_o. However, the triangular periodic orbits with an incident angle of $\pi/6$, as shown in Fig. 1(d), should be considered in a hexagonal microcavity with $n_i/n_o > 2$ as these light rays can also be totally reflected [94–96]. The solid lines in Fig. 1(d) indicate two isolated equilateral-triangular ray trajectories connecting the midpoints of secondary neighbor sides, with the shapes of an upright triangle "Δ" and a reversed triangle "∇". The dashed lines indicate ray trajectories in the same orbit family with lengths twice those of the solid lines. The triangular periodic orbits in the hexagonal microcavity are very similar to the periodic orbits in the equilateral-triangular microcavity [68,97]. The difference is that the triangular periodic orbits in the hexagonal microcavity are doubly degenerated.

In addition, the light rays reflected by the opposite sides with an incident angle of 0 also form triply degenerate periodic orbits, which are neglected in this paper because these light rays cannot be totally reflected. Overall, there are three families of periodic orbits in hexagonal microcavities with degeneracies of 1, 2, and 3. The numbers and degeneracies of periodic orbits in general polygonal microcavities are given in Ref. [75].

In hexagonal cavities with finite sizes, the incident angles on the sides are not exactly $\pi/3$ or $\pi/6$, considering the transverse

distribution of the periodic orbits. For a light ray with an initial incident angle (θ_b) other than 0, $\pi/6$, and $\pi/3$, the subsequent incident angles θ_i cannot remain unchanged but take only a few values. Here, the light rays in the clockwise (CW) and counterclockwise (CCW) directions are not distinguished. Then θ_i is restricted in the range of 0 to $\pi/2$, and all possible incident angles, θ_i, are given by

$$\theta_i = \begin{cases} \theta_b, 2\pi/3 - \theta_b, \theta_b - \pi/3; & \pi/3 < \theta_b < \pi/2 \\ \theta_b, \pi/3 - \theta_b, 2\pi/3 - \theta_b; & \pi/6 < \theta_b < \pi/3. \\ \theta_b, \pi/3 - \theta_b, \pi/3 + \theta_b; & 0 < \theta_b < \pi/6 \end{cases} \quad (1)$$

In general, there are three different incident angles θ_1, θ_2, and θ_3 within the ranges of $(0, \pi/6)$, $(\pi/6, \pi/3)$, and $(\pi/3, \pi/2)$, respectively, satisfying $\theta_1 + \theta_2 = \pi/3$ and $\theta_2 + \theta_3 = 2\pi/3$. For light rays near the hexagonal periodic orbits with a small offset angle of $\Delta\theta$ from $\pi/3$, the three incident angles are $\Delta\theta$ and $\pi/3 \pm \Delta\theta$. This means that the light ray shown by the solid line in Fig. 1(c) is slowly diverging from the center and will reach the corner on its other side with an incident angle of $\Delta\theta$ after finite times of reflection. The small incident angle of $\Delta\theta$ below the TIR condition results in pseudo-integrable leakage. For light rays near the triangular periodic orbits with a small offset angle of $\Delta\theta$ from $\pi/6$, the three incident angles are $\pi/2 - \Delta\theta$ and $\pi/6 \pm \Delta\theta$. All the three incident angles are above the TIR condition in the hexagonal microcavity with $n_i/n_o > 2$.

Another type of loss is boundary wave leakage [63]. However, for the high-Q superscar modes in regular polygonal microcavities, boundary wave leakage is relatively weak due to destructive interference between light waves with different incident angles at the boundaries, similar to that in the equilateral-triangular and square microcavities. For the hexagonal periodic orbits and triangular periodic orbits, destructive interference results from light waves with two incident angles of $\pi/3 \pm \Delta\theta$ and $\pi/6 \pm \Delta\theta$, respectively. Although the boundary wave leakage of light with incident angle near $\pi/6$ should be larger than that of light with incident angle near $\pi/3$, the destructive interference can minimize the boundary wave leakage.

In addition, the width of the rectangle formed by the triangular periodic orbits is larger than that of the rectangle formed by the hexagonal periodic orbits, leading to a smaller offset angle $\Delta\theta$ and lower scattering loss at the corners for the triangular periodic orbits [94]. Taking the pseudo-integrable leakage into account, WGMs corresponding to the hexagonal periodic orbits do not necessarily have higher Q than those corresponding to the triangular periodic orbits, and, thus, both kinds of WGMs should be considered in the analyses and simulations.

For a hexagonal microcavity with dimension much larger than the optical wavelength, the resonance conditions for the above two kinds of WGMs can be derived under the semi-classical approximation. During TIR at the sidewalls, a polarization-dependent negative phase shift occurs as

$$\delta(\theta) = -2 \arctan\left(\frac{\beta\sqrt{n_i^2 \sin^2\theta - n_o^2}}{n_i \cos\theta}\right), \quad (2)$$

where θ is the incident angle, and β equals 1 and n_i^2/n_o^2 for TM and TE polarized modes, respectively. For WGMs corresponding to the hexagonal periodic orbits (denoted as hexagonal WGMs for short), the round-trip length is $3\sqrt{3}a$ as shown in Fig. 1(c); then the resonance condition can be written as

$$\mathrm{Re}\left(3\sqrt{3}n_i ka\right) + 6\delta\left(\frac{\pi}{3}\right) = 2l\pi, \quad (3)$$

where k is the wavenumber in vacuum and l is the longitudinal mode number. For WGMs corresponding to the triangular periodic orbits (denoted as triangular WGMs for short), the ordinary round-trip length is $9a$ as shown by dashed lines in Fig. 1(d). The resonance condition for the triangular periodic orbits is generally written as

$$\mathrm{Re}(9n_i ka) + 6\delta\left(\frac{\pi}{6}\right) = 2l\pi. \quad (4)$$

The transverse mode number and longitudinal mode number of the triangular WGMs should have the same parity. Otherwise, it will lead to a trivial solution with the all-zero fields in the cavities similar to those in the equilateral-triangular microcavities [68]. Thus, the mode interval of the fundamental transverse triangular WGMs should be twice that obtained in Eq. (4) corresponding to an effective round-trip length of $9a/2$, similar to the solid lines shown in Fig. 1(d).

B. Symmetry Analyses and Mode Coupling

The group theory was used to analyze the symmetry of the modes in a hexagonal microcavity [73]. The symmetry of a regular hexagonal microcavity can be described by the point group C_{6v} as shown in Fig. 1(b). The point group C_{6v} includes a rotational subgroup $C_6 = \{E, C_6^1, C_6^2, C_6^3, C_6^4, C_6^5\}$, three mirror elements relative to the line connecting the midpoints of opposite sides σ_o, and three mirror elements relative to the diagonals σ_d. The character of the point group C_{6v} is listed in Table 1. The point group C_{6v} has four 1D and two 2D irreducible representations. The mode field distributions in the hexagonal microcavity should be classified into the irreducible representations of the point group.

The degeneracy of the WGMs should strictly fulfill the symmetry of the hexagonal microcavity. The WGMs in a hexagonal microcavity typically have multiple angular components with a difference of 6. WGMs with the angular components $6m$ and $6m + 3$ are non-degenerate standing-wave modes, which form A and B representations, respectively, where m is an integer. WGMs with the angular components $6m + 1$ and $6m + 5$ ($6m + 2$ and $6m + 4$) are double-degenerate modes, which form E_1 (E_2) representation. The E_1 (E_2) representation formed by double-degenerate modes can be expressed as two traveling-wave modes with the angular components $6m + 1$

Table 1. Character Table of Point Group C_{6v}

	E	C_6^1 (C_6^5)	C_6^2 (C_6^4)	C_6^3	$3\sigma_o$	$3\sigma_d$
A_1	1	1	1	1	1	1
A_2	1	1	1	1	−1	−1
B_1	1	−1	1	−1	1	−1
B_2	1	−1	1	−1	−1	1
E_1	2	−1	1	−2	0	0
E_2	2	1	−1	2	0	0

or $6m+5$ ($6m+2$ or $6m+4$), and can also be expressed as two standing-wave modes with both the angular components $6m+1$ and $6m+5$ ($6m+2$ and $6m+4$).

For WGMs corresponding to the hexagonal periodic orbits, the modes obviously follow the symmetry analyses above. For WGMs corresponding to the triangular periodic orbits, the situation will be slightly complicated, as these modes exhibit quadruple degeneracy according to the light rays shown in Fig. 1(d). Part of the degeneracy results from the CW and CCW propagation directions, similar to the WGMs in the equilateral-triangular microcavity; the other part of the degeneracy results from the double-degenerate "Δ" and "∇" periodic orbits in the hexagonal microcavity. According to the group theory analyses, the quadruple-degenerate modes become four non-degenerate standing-wave modes forming A_1, A_2, B_1, and B_2 representations, or two groups of double-degenerate modes forming E_1 and E_2 representations, depending on the angular components of the modes. The non-degenerate modes will have different mode Q factors.

The physical mechanism of removal of the degeneracy resulting from the double-degenerate "Δ" and "∇" periodic orbits can be understood by the mode coupling theory. In the scheme of ray optics, triangular periodic orbits "Δ" with a small offset angle, $\Delta\theta$, slowly diverge from the stable periodic orbits. After some time, they will cross the corner to the adjacent side, and then become triangular periodic orbits "∇". Thus, considering the offset of the incident angle, the two triangular periodic orbits are no longer isolated from each other; this results in coupling between the two kinds of triangular WGMs. In fact, mode coupling always occurs for modes with leakage unless it is forbidden by the cavity symmetry. The external coupling will lead to two modes with enhanced and reduced Q factors, corresponding to the destructive and constructive interference of the loss channels [94,98,99].

C. Numerical Simulation of WGMs in Hexagonal Microcavities

For a 2D hexagonal microcavity with a refractive index distribution of $n(x,y)$, the Maxwell equations for the confined optical field can be replaced with the scalar wave equation

$$-\nabla^2\psi(x,y) = n^2(x,y)\frac{\omega^2}{c^2}\psi(x,y), \tag{5}$$

where ω is the angular frequency, c is the light speed in vacuum, and ψ represents the field distribution. The WGMs in hexagonal microcavities are simulated by the finite-element method (commercial software—COMSOL Multiphysics 5.0) for revealing their mode characteristics. In the 2D microcavities, the TE and TM modes are simulated separately. A perfect matching layer is used to absorb the outgoing waves terminating the simulation window. The eigenvalues (ka) obtained in the hexagonal microcavities are complex numbers. The real parts of ka give the mode frequencies, and the Q factors can be obtained as $Q = \mathrm{Re}(k)/2|\mathrm{Im}(k)|$.

Figure 2(a) shows the simulated mode Q factors and normalized frequencies, $\mathrm{Re}(ka)$, of the TE modes in a hexagonal microcavity with $n_i/n_o = 3.2/1$. The transverse order is defined as the node number of the field distribution envelope along one sidewall, similar to that in the equilateral-triangular and square microcavities for high-Q superscar WGMs. The fundamental transverse (0th) WGMs corresponding to the hexagonal periodic orbits have Q factors ranging from 1200 to 2300. The magnetic-field amplitude distribution of one hexagonal WGM [A in Fig. 2(a)] is shown in Fig. 2(b).

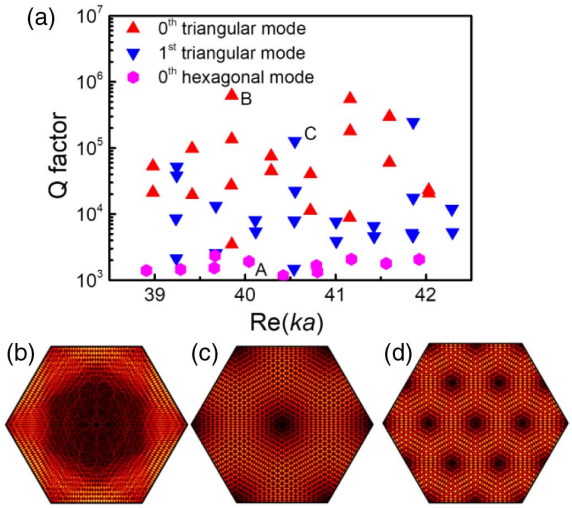

Fig. 2. (a) Simulated TE modes in the hexagonal microcavity with refractive indices of 3.2/1. (b)–(d) The magnetic-field amplitude distributions of the modes marked by A, B, and C.

There are a lot of modes with Q factors much higher than those of hexagonal WGMs. Based on the field distribution, these modes are denoted as triangular WGMs as they propagate along the triangular periodic orbits. As shown in Fig. 2(a), the 0th triangular WGMs have relatively high Q factors, and the mode with the highest Q is marked as mode B. Figure 2(c) shows the magnetic-field amplitude distribution of mode B, which indicates mixed fields of the "Δ" and "∇" triangular WGMs due to mode coupling. The mode interval of the 0th triangular WGMs is about 15% larger than those of the hexagonal WGMs, consistent with the interval ratio of $2\sqrt{3}/3$, which is derived from the reciprocal of half of the round-trip length ratio owing to the absence of odd longitudinal modes for the 0th triangular WGMs. Two high-Q modes are found at $ka = 39.85$ and 41.16, where the degeneracies of the modes are fully removed, and the WGMs are non-degenerate standing-wave modes with the angular component $3m$. The other modes appear as two double-degenerate mode pairs with two different Q factors because of mode coupling between the "Δ" and "∇" triangular WGMs; this removes the degeneracy induced by the double-degenerate periodic orbits [94]. For the triangular WGMs with the angular component $3m$, the degeneracy resulting from the CW and CCW propagation directions is also removed due to cavity-geometry-induced coupling or scattering between the two directions. The numerical simulation results are consistent with the symmetry analyses.

In the hexagonal microcavity, the first-order (1st) triangular WGMs can also have much higher Q factors than the hexagonal WGMs as shown in Fig. 2(a). The 1st triangular WGMs appear at the center between two 0th triangular WGMs, as they have odd and even longitudinal mode numbers. Three groups

of non-degenerate standing-wave modes with high Q factors are found at $ka = 39.24$, 40.55, and 41.86. Figure 2(d) shows the magnetic-field amplitude distribution of a non-degenerate 1st triangular WGM [C in Fig. 2(a)]. Considering the 1st triangular WGMs, the mode interval of the triangular WGMs is much smaller than those of the hexagonal WGMs, which agrees well with Eqs. (3) and (4) with a round-trip length ratio of $3/\sqrt{3}$.

To further demonstrate the mode properties of the WGMs in hexagonal microcavities, cavities with different refractive index ratios, n_i/n_o, are considered. Figure 3(a) shows the simulated mode Q factors and normalized frequencies, Re(ka), of the TE modes in a hexagonal microcavity with $n_i/n_o = 3.2/1.54$. The 0th hexagonal WGMs have the highest Q, ranging from 1300 to 2200, which is almost the same as those of the hexagonal WGMs in the microcavity with $n_i/n_o = 3.2/1$. The mode Q factors of the triangular WGMs are lower than 1000 due to high boundary wave leakage as the incident angle of $\pi/6$ is only slightly higher than the TIR angle of 0.16π.

Figure 3(b) shows the simulated mode Q factors of mode A [shown in Figs. 2(a) and 3(a)] and mode B [shown in Fig. 2(a)] as functions of n_i/n_o. The Q factor of the hexagonal WGM (mode A) almost does not vary with refractive index ratio, indicating the dominant loss is pseudo-integrable leakage, which is insensitive to refractive index. The existence of pseudo-integrable leakage loss limits the Q factors of the hexagonal WGMs. On the contrary, the triangular WGMs have much higher Q factors in a hexagonal microcavity with a high refractive index ratio due to the absence of pseudo-integrable leakage. The numerical simulation results are consistent with the analyses of ray optics. The Q factor of the triangular WGM (mode B) shows an exponential decrease as $n_i/n_o < 2.6$. The possible reason is that, with decrease of n_i/n_o, boundary wave leakage increases, and the destructive interference between the two boundary waves with $\pi/6 \pm \Delta\theta$ also worsens as the smaller incident angle ($\pi/6 - \Delta\theta$) is close to the TIR angle. The results show that a hexagonal WGM or a triangular WGM dominates depending on the refractive index ratio of the hexagonal microcavity.

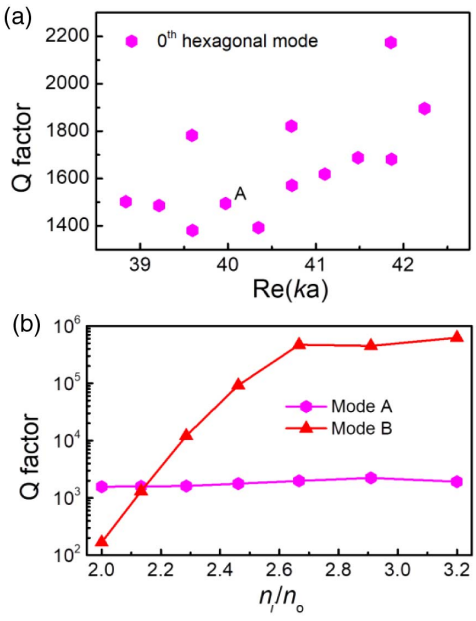

Fig. 3. (a) Mode Q factors versus normalized frequency for TE modes in the hexagonal microcavity with refractive indices of 3.2/1.54. (b) Simulated mode Q factors of modes A and B as functions of n_i/n_o.

D. WGMs in Wavelength-Scale Hexagonal Nanocavities

In wavelength-scale hexagonal nanocavities, WGMs cannot be described by the ray model, but can be simulated numerically [100]. The mode wavelengths obtained by Eq. (3) will be significantly larger than the actual values, because the propagation constants corresponding to transverse distributions are not taken into account. Both TE and TM modes are considered as they have distinct mode properties in wavelength-scale nanocavities. Every WGM in a hexagonal nanocavity has one main angular component, and, hence, it is denoted as $TE_{v,1}$ or $TM_{v,1}$ with the angular mode number v corresponding to the main component [73].

Figures 4(a) and 4(b) show, respectively, the mode Q factors of the $TE_{v,1}$ and $TM_{v,1}$ modes as functions of angular mode number v in a wavelength-scale hexagonal nanocavity with refractive indices of 3.2/1. The symmetries of the modes are defined based on the symmetries of the electric (magnetic-) field amplitude distributions relative to one diagonal for the TM (TE) modes. The Q factors of the WGMs in the wavelength-scale hexagonal nanocavity show a peak at $v = 6$.

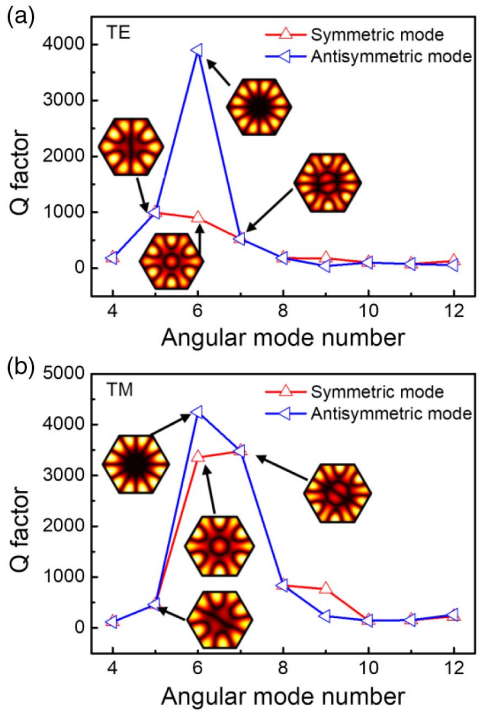

Fig. 4. Mode Q factors of (a) TE and (b) TM modes in a wavelength-scale hexagonal nanocavity with refractive indices of 3.2/1 as functions of angular mode number. The insets show, respectively, the magnetic- and electric-field amplitude distributions of the TE and TM modes.

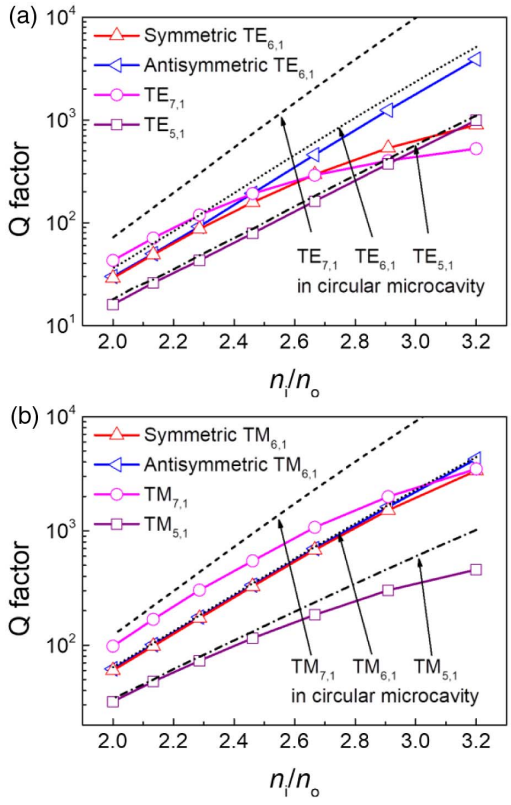

Fig. 5. Mode Q factors of (a) TE and (b) TM modes in the wavelength-scale hexagonal nanocavity as functions of n_i/n_o.

The non-degenerate antisymmetric $TE_{6,1}$ or $TM_{6,1}$ modes have the highest Q factors. A secondary high-Q mode appears at $v = 5$ and 7 for the TE and TM modes, respectively. The insets show the magnetic- and electric-field amplitude distributions of the TE and TM modes with $v = 5$, 6, and 7. TE modes with $v > 7$ and TM mode with $v > 9$ have Q factors about one order of magnitude lower than the peak value. The TM modes generally have higher Q factors than the TE modes, and the $TM_{v+1,1}$ and $TE_{v,1}$ modes have close resonant frequencies.

To characterize the WGMs in a hexagonal nanocavity fabricated with different material, Figs. 5(a) and 5(b) show, respectively, the mode Q factors of TE and TM modes with $v = 5$, 6, and 7 as functions of n_i/n_o in the wavelength-scale hexagonal nanocavity. The analytical Q factors of the TE and TM modes in a circular microcavity are presented as a comparison. With decrease of n_i/n_o, the modes with $v = 7$ become the modes with the highest Q among the four modes shown in Fig. 5. For the TE modes, the Q factors of the $TE_{5,1}$ and the antisymmetric $TE_{6,1}$ modes are, respectively, about 10% and 20% lower than those in the circular microcavity. For the TM modes, the Q factor of the antisymmetric $TM_{6,1}$ mode agrees very well with that in the circular microcavity. The Q factors of the WGMs in a hexagonal cavity with a small angular mode number are comparable to those in perfect circular cavities, which indicates that the hexagonal cavities are suitable for demonstrating nanocavity lasers with diagonal lengths close to the wavelength of light.

3. BOTTOM-UP GROWN HEXAGONAL MICRO-/NANOCAVITY LASERS

For WGM microcavities, a smooth surface is very important for achieving high-Q modes as it can eliminate the scattering loss during the TIR process. One interesting feature for hexagonal micro-/nanocavities is that the ZnO- or nitride-based semiconductor material for UV laser diodes generally has a wurtzite crystal structure and typically presents a natural hexagonal cross section with a smooth surface [77–82]. Based on GaAs material with a cubic zinc-blende structure, a hexagonal microcavity was also realized by selective area growth on a (111) substrate [101]. In addition, WGM lasing was achieved in zeolitic crystal-dye [102,103], metal-organic framework [104,105], and lead halide perovskite [96,106,107] hexagonal micro-/nanocavities. This paper mainly focuses on the hexagonal micro-/nanocavities formed by conventional semiconductors, such as ZnO and III–V compound semiconductor materials.

A. ZnO WGM Micro-/Nanocavity Lasers

Due to its hexagonal wurtzite structure, the grown micro-/nanostructure ZnO exhibits a hexagonal cross section supporting WGMs with TIR at the hexagonal facet. There are different types of structures in the direction perpendicular to the hexagonal plane (here defined as z axis), such as needles with varied diameters, nods with uniform size, and nails or disks with light confined in a thin slab due to high refractive index contrast in the z-direction. In the micro-/nanoneedles or nanonods, the WGMs are generally continuous states similar to those in optical fibers or microcylinders with near-zero propagation constants along z axis [18,19]; the WGMs are excited by selective area pumping to build an image refractive index distribution along z axis as gain waveguiding.

ZnO is a direct-bandgap semiconductor with a bandgap of about 3.4 eV for UV light emission. The bulk ZnO material commonly shows an additional unstructured luminescence band with a full width at half-maximum (FWHM) of ~600 meV and spectra maximum around 2.35 eV (≈530 nm) within the visible spectral range, due to oxygen or zinc vacancies. In 2004, Nobis *et al.* reported WGM resonances within the visible spectral range in hexagonal ZnO nanoneedles with diameters comparable to the wavelength of light, and symmetrically analyzed WGMs with angular mode numbers ranging from 1 to 6 in a single ZnO nanoneedle for the first time [64].

UV WGM lasing of ZnO hexagonal micro-/nanocavities was first reported by Wang *et al.* in 2006 from optically pumped ZnO nanonails [83]. The nanonail was composed of a long nanorod and a hexagonal head. The nanonails had structures similar to that of typical WGM microdisks on a post. The lasing threshold was about 17 MW/cm^2 and the FWHMs of the peaks were 0.08 nm. Multiple lasing peaks were observed in the spectra as multiple nanonails were excited by pumping laser light with a spot 10 μm in diameter. Through an in-depth discussion of the possible lasing mechanism, the lasing modes were attributed to WGMs because the other types of modes should have had much lower Q factors.

In 2010, Gargas *et al.* reported single-mode lasing in individual ZnO hexagonal nanodisks with diameters (measured

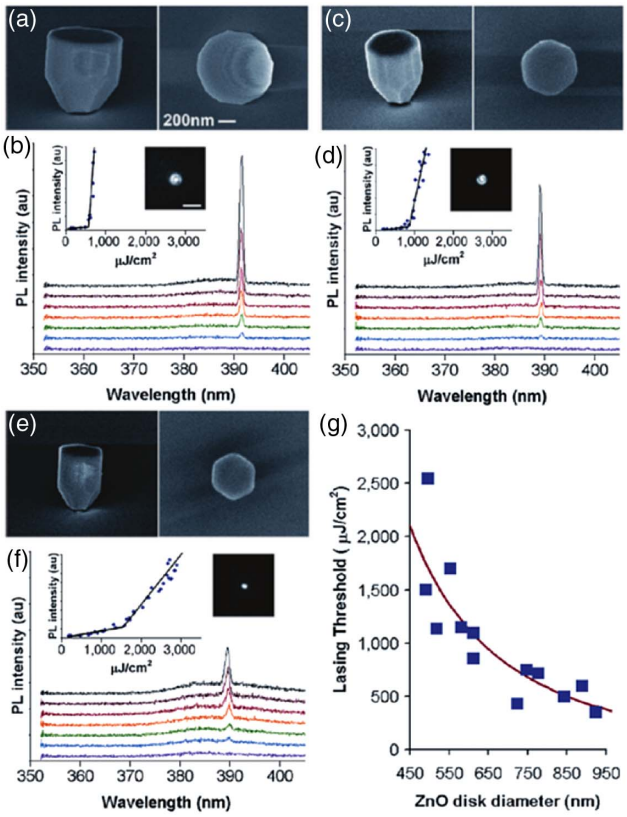

Fig. 6. Cross-section and top-down SEM images of ZnO nanodisks with diameters of (a) 842 nm, (c) 612 nm, and (e) 491 nm. (b), (d), and (f) Corresponding lasing spectra collected at increasing pump powers. Inset: PL intensity versus pump power. (g) Room temperature lasing threshold versus disk diameter. Reproduced from Ref. [80].

edge to edge) from 280 to 900 nm [80]. WGM lasing was achieved in subwavelength ZnO hexagonal nanodisks, and the lasing modes can be well explained by a 3D finite-difference time-domain (FDTD) numerical simulation. These nanodisks were relatively thick, with heights of several hundreds of nanometers, supporting high-order modes in the vertical direction. Figures 6(a), 6(c), and 6(e) show, respectively, the cross-section and top-down scanning electron microscope (SEM) images of ZnO hexagonal nanodisks with diameters of 842, 612, and 491 nm. Figures 6(b), 6(d), and 6(f) show, respectively, the lasing spectra collected at increased pump powers for the corresponding nanodisks in Figs. 6(a), 6(c), and 6(e). The lasing spectra indicate single-mode lasing at room temperature. Figure 6(g) shows the lasing threshold at room temperature versus nanodisk diameter. The best-fit line (red curve) is approximately $1/D^2$, which suggests the dependence of lasing threshold on nanodisk diameter. For ZnO nanodisks with diameters of 375 and 283 nm, WGM lasing was realized at a low temperature of 8 K.

In 2011, Chen *et al.* reported room-temperature WGM lasing in ZnO hexagonal microdisks with diameters from ~2 μm up to ~14 μm [86]. Due to the relatively large size, multiple lasing peaks appeared in the spectra. The intervals agree well with the theoretical values of the longitudinal-mode intervals of the WGMs, which indicates that the observed peaks corresponded to the WGMs.

Compared with micro-/nanonails or nanodisks, wire- or rod-like ZnO can be easily grown by the vapor-phase transport method. Czekalla *et al.* observed WGM lasing in 2008 from an individual ZnO microrod under optical pumping at a temperature of 10 K with a lasing threshold of 170 kW/cm^2 [79]. The lasing peaks observed agreed well with the WGM positions predicted by a plane wave model for microrods with diameters ranging from 3 to 12 μm.

In 2009, Xu's group demonstrated WGM lasing from an individual ZnO microrod at room temperature under two-photon excitation by a femtosecond pulse laser with a wavelength of 800 nm [85], and subsequently pumped by a nanosecond Nd:YAG laser operating at 355 nm [84]. Figure 7(a) shows the emission spectra of the ZnO microrod with a diagonal of 6.67 μm excited by a Nd:YAG laser at different excitation power densities. Two evident peaks appear in the emission spectrum at an excitation power density of 255 kW/cm^2. More peaks appear with FWHMs of about 0.3 nm, and peak intensities increase dramatically as the excitation power is further increased to 320 kW/cm^2, indicating a transition from spontaneous emission to stimulated emission. Figure 7(b) shows output power as a function of the excitation power density. Output power increases slowly and dramatically as the excitation power density is lower and higher than 255 kW/cm^2, respectively, which is also an evidence of lasing.

Electrically pumped lasing is always an interesting topic for practical applications of these semiconductor lasers. In 2011, Dai *et al.* fabricated an n-ZnO microrod/p-GaN heterojunction for current injection and demonstrated electrically pumped WGM lasers [108]. Recently, subsequent in-depth researches were conducted on ZnO WGM microrod lasers—e.g., an electrically pumped ZnO WGM microlaser array [109,110], single-mode lasing in coupled microrods with the Vernier effect [111], and plasmon-enhanced WGM lasing in ZnO microrods [112,113] were demonstrated.

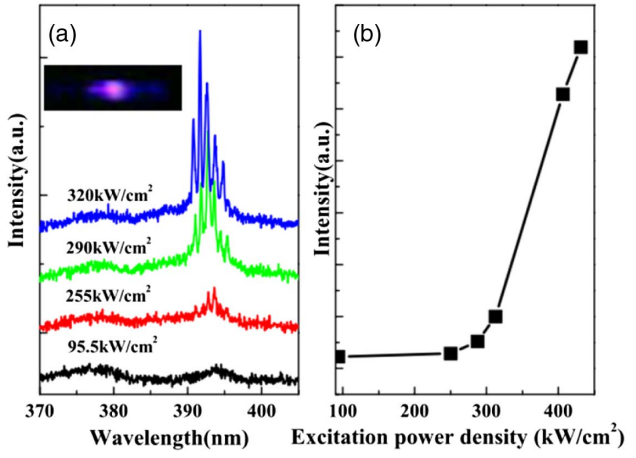

Fig. 7. (a) Emission spectra of a ZnO microrod with a diagonal of 6.67 μm when excited with a Nd:YAG laser at different excitation power densities. Inset: far-field emission image of the lasing ZnO microrod taken with a digital camera. (b) Output lasing intensity versus excitation power density. Reproduced from Ref. [84].

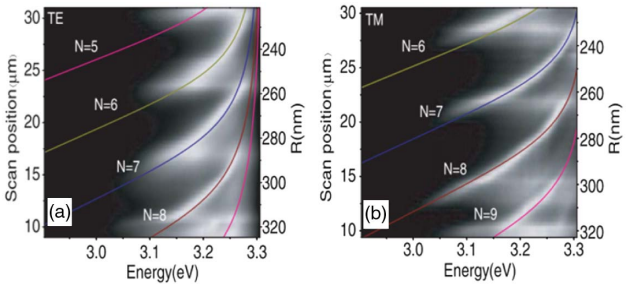

Fig. 8. PL mapping along the ZnO tapered arm for (a) TE and (b) TM polarized modes. Reproduced from Ref. [119].

The lasing mechanism in the ZnO hexagonal micro-/nanocavities above can be explained as exciton lasing. The electron–hole binding energy is about 60 meV for ZnO, and the excitons are thus stable at room temperature. In a high-quality cavity, if the cavity modes are strongly coupled with the excitons, a new kind of bosonic quasi-particle, the exciton–polariton, will be generated. Ultralow-threshold lasing is expected in the exciton–polariton system [114–117]. Van Vugt *et al.* reported strong exciton–photon coupling in ZnO nanonods at room temperature in 2006 [118]. Two groups of polariton modes with Rabi splitting of more than 100 meV were observed.

In 2008, Sun *et al.* reported exciton–polariton WGMs from a tapered ZnO hexagonal nanocavity [119]. Figures 8(a) and 8(b) show, respectively, the photoluminescence (PL) spectra of the TE and TM modes in a tapered ZnO WGM nanocavity with hexagonal side length (R) ranging from 320 to 220 nm. With decrease of the size of the hexagonal cross section, the modes blue-shift. When the modes approach the exciton energy, the coupling between the excitons and the WGM photons becomes intensive, resulting in an exciton–polariton. The solid lines denote the theoretical lower branches of the WGM mode polaritons according to exciton–polariton dispersion. In the ZnO microrods, the WGMs are continuous states and exhibit a parabolic-like dispersion relative to the propagation constant in z axis (k_z, or called momentum) [120]. Thus, strong coupling between an exciton and a photon can be realized in such cavities using an angle-resolved PL spectroscopy technique. The lasing of an exciton–polariton can be confirmed by the condensation of the polaritons in the angle-resolved PL spectra. Polariton condensation and WGM mode polariton lasing in microrods were demonstrated at up to 450 K in Refs. [115,121,122].

B. III–V WGM Micro-/Nanocavity Lasers

GaN is another attractive direct-bandgap semiconductor material for realizing a UV light emitter with a hexagonal wurtzite structure. In 1997, Akasaka *et al.* grew a GaN hexagonal microstructure on a sapphire substrate using metal-organic chemical vapor deposition with a patterned GaN epitaxial layer [93]. The GaN grown micro-/nanostructures can maintain high crystal quality owing to strain relaxation due to their small sizes during the epi-growth process [81,123]. Apart from the improved material qualities, the smooth GaN facets would act as TIR mirrors for confining WGMs. Thus, Tessarek *et al.* observed WGMs and corresponding stimulated emission with

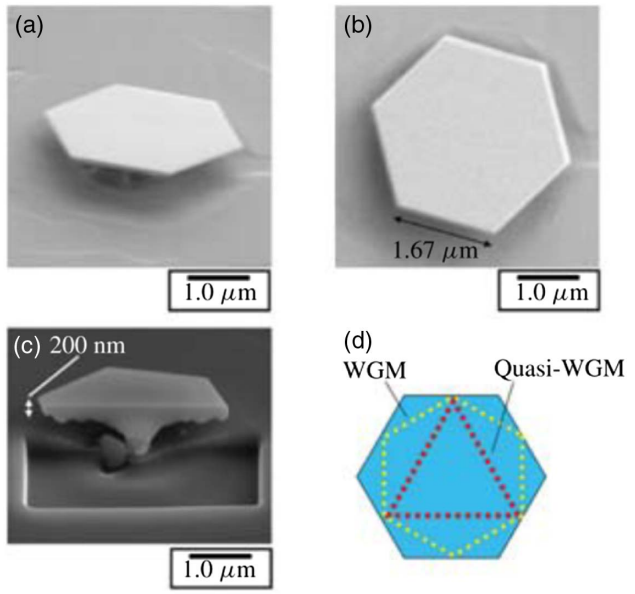

Fig. 9. SEM images of (a) the bird's-eye view and (b) the top view of a GaN hexagonal microdisk. (c) Bird's-eye-view SEM image of the GaN hexagonal microdisk cut with an FIB. (d) Schematic diagram of hexagonal and triangular periodic orbits (called WGM and quasi-WGM here). Reproduced from Ref. [87].

the threshold above 1.1 MW/cm^2 from GaN hexagonal microrods [82,124–126].

In 2011, Kouno *et al.* grew GaN microdisks supported by small posts using RF-plasma-assisted molecular beam epitaxy [87]. Compared with microrods, the microdisks have high refractive index contrast in the direction perpendicular to the hexagonal plane, which can enhance the confinement of WGMs for realizing high Q factors. Due to the fast lateral growth, free-standing GaN hexagonal microdisks were formed on the small posts. Figures 9(a) and 9(b) show, respectively, the bird's-eye-view and top-view SEM images of a GaN hexagonal microdisk, and Fig. 9(c) shows a cross-sectional-view SEM image of a GaN hexagonal microdisk cut with a focused ion beam (FIB), exhibiting a thickness of ~200 nm. UV lasing at a wavelength of 372 nm was demonstrated with a Q factor of 700 at a lasing threshold of 250 kW/cm^2. The lasing modes were found to be triangular WGMs (as the quasi-WGM shown in Fig. 9) based on numerical simulations [87,95].

Hexagonal micro-/nanostructures can also be grown using GaAs material with cubic zinc-blende structure on a (111) substrate [101]. Nowadays, integrating III–V materials on silicon substrate has become an important research area for realizing active optoelectronic devices integrated with Si electronics. In 2009, Moewe *et al.* grew core–shell InGaAs/GaAs quantum well nanoneedles on silicon [127].

Based on the core–shell InGaAs/GaAs hexagonal structures, Chen *et al.* reported WGM nanopillar lasers grown on silicon in 2011 [128]. These lasers offered tiny footprints and scalability, and, thus, were suited to high-density photonic integration. Figure 10(a) shows the ray path in an on-chip nanopillar. The incident angle on the substrate can be smaller than the TIR angle, supporting light confinement in the vertical

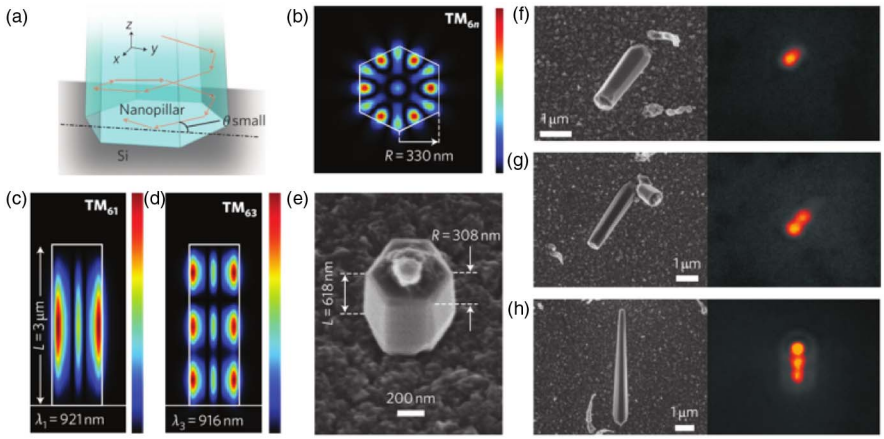

Fig. 10. (a) Schematic diagram of ray path in on-chip nanopillars. (b) FDTD-simulated field profile of a WGM with an angular mode number of 6 in the hexagonal plane. (c) First-order and (d) higher-order transverse modes in the vertical direction. (e) SEM image of a subwavelength device. [(f)–(h)] SEM images and experimental emission patterns of nanopillars. Reproduced from [128].

direction as the light mainly propagates in the horizontal plane. Figure 10(b) shows the FDTD-simulated field profile of a WGM with an angular mode number of 6 in the hexagonal horizontal plane. Figures 10(c) and 10(d) show, respectively, the field distributions of the first-order and higher-order transverse modes in the vertical direction (along the nanopillar). Figure 10(e) shows the SEM image of a subwavelength device. Figures 10(f)–10(h) show, respectively, the SEM images and experimental emission patterns of nanopillar lasers, which indicate a standing-wave pattern along the nanopillars, agreeing well with the numerical simulations.

4. TOP-DOWN FABRICATED HEXAGONAL MICROCAVITY LASERS

With the top-down fabrication technology, hexagonal microcavities of controllable sizes and geometries can be formed. For instance, GaN [129] and molecular single-crystalline [90] hexagonal microcavity arrays were fabricated using top-down processes. Waveguide-coupled unidirectional emission is necessary for practical application of WGM hexagonal microcavity lasers [130,131].

AlGaInAs/InP hexagonal microcavity lasers with an output waveguide butt-coupled to one vertex of the hexagon were fabricated on a multiple-quantum-well epitaxial laser wafer using the standard planar fabrication technology [89]. The waveguide-coupled hexagonal microcavity semiconductor lasers were suitable for photonic integrated circuits and optical interconnects. The inset in Fig. 11(a) shows a microscope image of a fabricated hexagonal microcavity laser with a side length of 10 μm and an output waveguide width of 1.5 μm. The hexagonal microcavity lasers were mounted on a thermoelectric cooler (TEC) to control the substrate temperature. Figure 11(a) shows the multimode-fiber-coupled light power and applied voltage versus continuous-wave injection measured at a TEC temperature of 288 K. The threshold current is about 6 mA, corresponding to a current density of 2.3 kA/cm^2. Figure 11(b) shows the lasing spectra at injection currents of 6, 30, and 55 mA, where single-mode operation was

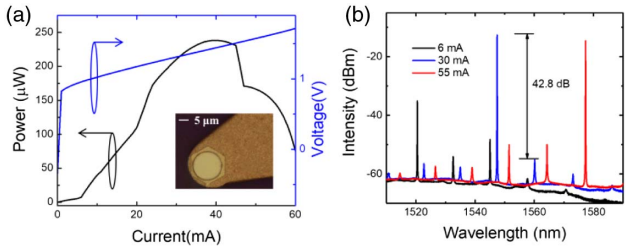

Fig. 11. (a) Applied voltage and fiber-coupled output power versus continuous-wave injection current, and (b) lasing spectra at different injection currents for a hexagonal microcavity laser with a side length of 10 μm and a 1.5-μm-wide output waveguide. The inset in (a) shows a microscopic image of the hexagonal microcavity laser.

achieved with a side mode suppression ratio (SMSR) of 42.8 dB at the injection current of 30 mA.

Although the hexagonal microcavity lasers exhibit excellent single-transverse-mode property as shown in Fig. 11(b), the Q factors of the WGMs in a hexagonal microcavity are much lower than those of the WGMs in a circular microcavity of similar size. Especially for a hexagonal microcavity with weak refractive index contrast, the Q factors of the WGMs are very low as shown in Fig. 3(a). Center holes and round corners were introduced for improving the mode Q factors [72,88]. Recently, the mode Q factors of WGMs in square microcavities were enhanced by replacing the flat sides with circular arcs, and the lasing spectra were engineered by tuning the deformation parameters [71,132,133].

To enhance the Q factors of WGMs, AlGaInAs/InP deformed hexagonal microcavity lasers were proposed with the flat sides replaced with circular arcs [91]. Low-threshold lasing was demonstrated while the single-transverse-mode property was maintained. Figure 12(a) shows an SEM image of a waveguide-coupled deformed hexagonal microcavity laser after dry etching of the laser cavity. Figure 12(b) shows a microscope image of a fabricated deformed hexagonal microcavity laser. The devices were cleaved over the output waveguide leaving

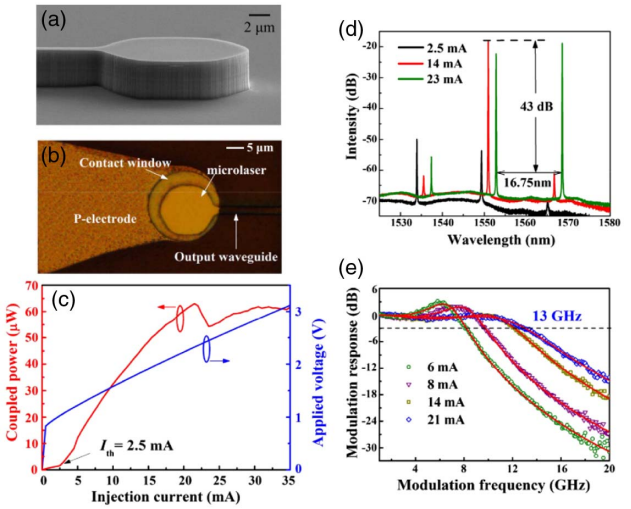

Fig. 12. (a) SEM image of a deformed hexagonal microlaser after inductively coupled plasma etching. (b) Microscopic image of a deformed hexagonal microcavity laser. (c) Applied voltage and fiber-coupled output power versus continuous-wave injection current. (d) Lasing spectra at injection currents of 2.5, 14, and 23 mA. (e) Small-signal responses for the circular-side hexagonal resonator at bias currents of 6, 8, 14, and 21 mA. Reproduced from Ref. [91].

a length of ~10 μm, and bonded on an AlN submount with a thin-film resistance of 30 Ω in series to match the impedance to ~50 Ω. For the waveguide-coupled deformed hexagonal microcavity laser with a side length $a = 7.5$ μm, circular arc radius of $R = 14$ μm, and output waveguide width of $d = 2$ μm, the multimode-fiber-coupled output power and applied voltage versus continuous-wave injection current are measured at a temperature of 288 K and are plotted in Fig. 12(c). The threshold current is about 2.5 mA with a current density of 1.5 kA/cm^2, and the maximum coupled output power is 63 μW at 21 mA. Compared with the non-deformed hexagonal microcavity laser, the lasing threshold current density is much lower owing to the enhanced mode Q factors. Figure 12(d) shows the lasing spectra at injection currents of 2.5, 14, and 23 mA, where three fundamental transverse modes are found around 1535.54, 1550.95, and 1566.67 nm, and a very wide first-order transverse mode is found around 1560 nm at 14 mA. Single-mode operation is demonstrated with an SMSR of 43 dB at 14 mA. Figure 12(e) shows the small-signal modulation responses of the waveguide-coupled deformed hexagonal microcavity laser at different bias currents. The 3 dB bandwidth increases from 8.2 to 13.0 GHz as the bias current is increased from 6 to 21 mA, and the resonance peak height decreases from 3.0 to below 0.2 dB showing a very flat response curve as the bias current exceeds 14 mA.

Apart from single-mode lasing, the deformation provides another parameter to control WGMs inside microcavities. The transverse mode intervals can be controlled by the deformation parameters as different transverse modes have different round-trip lengths [71,132]. In addition, the wavelength interval can be tuned by adjusting the injection current, as different modes have different field distributions, similar to that in a square microcavity [134]. Nonlinear dynamics, including chaos, four-wave mixing, and high-order oscillations states, are observed based on the deformed hexagonal microlaser. Random bits are generated based on the same laser under chaos state without external optical injection or feedback [135].

5. SUMMARY AND OUTLOOK

In summary, progress in WGM hexagonal micro-/nanocavity lasers has been reviewed, particularly for hexagonal semiconductor lasers. The semi-classical ray model is introduced to analyze WGMs in hexagonal microcavities of relatively large sizes. Accordingly, the WGMs are divided into hexagonal and triangular WGMs. The symmetry properties of the hexagonal cavities are described by the point group C_{6v}, which reveal the degeneracy of the confined modes. Mode coupling occurs between degenerate triangular WGMs belonging to different triangular periodic orbits, and results in the removal of mode degeneracy. The mode Q factors of the hexagonal and triangular WGMs show distinct dependences on the refractive index contrast of the hexagonal microcavities, and this can be well explained by the ray model. WGMs cannot be simply explained by the ray model in wavelength-scale hexagonal nanocavities because the transverse distributions of the light rays cannot be neglected. The field distributions of the WGMs in wavelength-scale hexagonal nanocavities are quite similar to those in circular microcavities, and the corresponding mode Q factors are not necessarily positively related to the angular mode number. Semiconductor materials with a wurtzite crystal structure, such as ZnO or III–V semiconductors, can present a natural hexagonal cross section in bottom-up grown processes, where the smooth boundaries can reduce the scattering loss effectively and ensure high Q factors of the WGMs. Hexagonal micro-/nanocavity lasers synthesized using various materials, cavity structures, and lasing mechanisms have been demonstrated successfully. Furthermore, controllable deformation can be introduced in top-down fabrication processes, which allows lasing-mode manipulation and waveguide-coupled unidirectional emission. By replacing the flat sides with circular arcs, the Q factors of the WGMs can be greatly enhanced for low-threshold lasing. Deformed hexagonal microcavity semiconductor lasers were also demonstrated for high-speed direct modulation, dual-transverse mode lasing, and random bit generation.

Compared with circular cavities, hexagonal micro-/nanocavities exhibit relatively lower Q factors but distinct mode properties for the WGMs. The unique properties of the WGMs in the hexagonal micro-/nanocavities, such as field distributions, mode structures, symmetries, and degeneracies, allow further regulation of the WGMs through cavity deformation, spatially selective current injection, and output waveguide coupling, for practical application of the hexagonal lasers. Moreover, naturally synthesized hexagonal micro-/nanocavities with smooth surface faceting and high Q factors can be used for realizing compact-size low-threshold UV laser diodes, and the enhanced light–matter interaction in these cavities also opens a way to study the physical properties of the corresponding materials. Therefore, corresponding research works on hexagonal micro-/nanocavity lasers play a significant role in both fundamental physics studies and potential device applications. Multiple functional laser devices based on WGM hexagonal

micro-/nanocavities have already been demonstrated. The performance of these lasers can be improved and practical application can be realized through further research.

Funding. Key Research Program of Frontier Sciences, Chinese Academy of Sciences (QYZDJ-SSW-JSC002); National Natural Science Foundation of China (NSFC) (61527823, 61875188).

REFERENCES

1. K. J. Vahala, "Optical microcavities," Nature **424**, 839–846 (2003).
2. J. Ward and O. Benson, "WGM microresonators: sensing, lasing and fundamental optics with microspheres," Laser Photon. Rev. **5**, 553–570 (2011).
3. L. N. He, S. K. Ozdemir, and L. Yang, "Whispering gallery microcavity lasers," Laser Photon. Rev. **7**, 60–82 (2013).
4. V. D. Ta, R. Chen, L. Ma, Y. J. Ying, and H. D. Sun, "Whispering gallery mode microlasers and refractive index sensing based on single polymer fiber," Laser Photon. Rev. **7**, 133–139 (2013).
5. J. Wang, T. R. Zhan, G. S. Huang, P. K. Chu, and Y. F. Mei, "Optical microcavities with tubular geometry: properties and applications," Laser Photon. Rev. **8**, 521–547 (2014).
6. H. Cao and J. Wiersig, "Dielectric microcavities: model systems for wave chaos and non-Hermitian physics," Rev. Mod. Phys. **87**, 61–111 (2015).
7. X. F. Jiang, C. L. Zou, L. Wang, Q. H. Gong, and Y. F. Xiao, "Whispering-gallery microcavities with unidirectional laser emission," Laser Photon. Rev. **10**, 40–61 (2016).
8. X. F. Jiang, L. B. Shao, S. X. Zhang, X. Yi, J. Wiersig, L. Wang, Q. H. Gong, M. Loncar, L. Yang, and Y. F. Xiao, "Chaos-assisted broadband momentum transformation in optical microresonators," Science **358**, 344–347 (2017).
9. J. W. Strutt and B. Rayleigh, "The problem of the whispering gallery," Phil. Mag. **20**, 1001–1004 (1910).
10. S. L. Mccall, A. F. J. Levi, R. E. Slusher, S. J. Pearton, and R. A. Logan, "Whispering-gallery mode microdisk lasers," Appl. Phys. Lett. **60**, 289–291 (1992).
11. A. F. J. Levi, R. E. Slusher, S. L. Mccall, S. J. Pearton, and W. S. Hobson, "Room-temperature lasing action in $In_{0.51}Ga_{0.49}P/In_{0.2}Ga_{0.8}As$ microcylinder laser-diodes," Appl. Phys. Lett. **62**, 2021–2023 (1993).
12. M. Cai, O. Painter, K. J. Vahala, and P. C. Sercel, "Fiber-coupled microsphere laser," Opt. Lett. **25**, 1430–1432 (2000).
13. S. J. Choi, K. Djordjev, S. J. Choi, and P. D. Dapkus, "Microdisk lasers vertically coupled to output waveguides," IEEE Photon. Technol. Lett. **15**, 1330–1332 (2003).
14. L. Yang, D. K. Armani, and K. J. Vahala, "Fiber-coupled erbium microlasers on a chip," Appl. Phys. Lett. **83**, 825–826 (2003).
15. E. P. Ostby, L. Yang, and K. J. Vahala, "Ultralow-threshold $Yb^{3+}:SiO_2$ glass laser fabricated by the solgel process," Opt. Lett. **32**, 2650–2652 (2007).
16. H. S. Rong, S. B. Xu, Y. H. Kuo, V. Sih, O. Cohen, O. Raday, and M. Paniccia, "Low-threshold continuous-wave Raman silicon laser," Nat. Photonics **1**, 232–237 (2007).
17. A. C. Tamboli, E. D. Haberer, R. Sharma, K. H. Lee, S. Nakamura, and E. L. Hu, "Room-temperature continuous-wave lasing in GaN/InGaN microdisks," Nat. Photonics **1**, 61–64 (2007).
18. Y. D. Yang, Y. Z. Huang, and Q. Chen, "High-Q TM whispering-gallery modes in three-dimensional microcylinders," Phys. Rev. A **75**, 013817 (2007).
19. Y. Z. Huang and Y. D. Yang, "Mode coupling and vertical radiation loss for whispering-gallery modes in 3-D microcavities," J. Lightwave Technol. **26**, 1411–1416 (2008).
20. H. S. Rong, S. B. Xu, Y. H. Kuo, V. Sih, O. Cohen, O. Raday, and M. Paniccia, "Whispering gallery mode lasing in electrically driven quantum dot micropillars," Appl. Phys. Lett. **97**, 101108 (2010).
21. Y. D. Yang, Y. Z. Huang, W. H. Guo, Q. Y. Lu, and J. F. Donegan, "Enhancement of quality factor for TE whispering-gallery modes in microcylinder resonators," Opt. Express **18**, 13057–13062 (2010).
22. Y. D. Yang, S. J. Wang, and Y. Z. Huang, "Investigation of mode radiation loss for microdisk resonators with pedestals by FDTD technique," Chin. Opt. Lett. **8**, 502–504 (2010).
23. J. K. Kitur, V. A. Podolskiy, and M. A. Noginov, "Stimulated emission of surface plasmon polaritons in a microcylinder cavity," Phys. Rev. Lett. **106**, 183903 (2011).
24. J. S. Levy, M. A. Foster, A. L. Gaeta, and M. Lipson, "Harmonic generation in silicon nitride ring resonators," Opt. Express **19**, 11415–11421 (2011).
25. Y. D. Yang and Y. Z. Huang, "Investigation of vertical leakage loss for whispering-gallery modes in microcylinder resonators," J. Lightwave Technol. **29**, 2754–2760 (2011).
26. W. Bogaerts, P. De Heyn, T. Van Vaerenbergh, K. De Vos, S. K. Selvaraja, T. Claes, P. Dumon, P. Bienstman, D. Van Thourhout, and R. Baets, "Silicon microring resonators," Laser Photon. Rev. **6**, 47–73 (2012).
27. R. Chen, V. D. Ta, and H. D. Sun, "Single mode lasing from hybrid hemispherical microresonators," Sci. Rep. **2**, 244 (2012).
28. M. Munsch, J. Claudon, N. S. Malik, K. Gilbert, P. Grosse, J. M. Gerard, F. Albert, F. Langer, T. Schlereth, M. M. Pieczarka, S. Hofling, M. Kamp, A. Forchel, and S. Reitzenstein, "Room temperature, continuous wave lasing in microcylinder and microring quantum dot laser diodes," Appl. Phys. Lett. **100**, 031111 (2012).
29. J. T. Lin, Y. X. Xu, J. X. Song, B. Zeng, F. He, H. L. Xu, K. Sugioka, W. Fang, and Y. Cheng, "Low-threshold whispering-gallery-mode microlasers fabricated in a Nd:glass substrate by three-dimensional femtosecond laser micromachining," Opt. Lett. **38**, 1458–1460 (2013).
30. S. Mehrabani and A. M. Armani, "Blue upconversion laser based on thulium-doped silica microcavity," Opt. Lett. **38**, 4346–4349 (2013).
31. L. X. Zou, Y. Z. Huang, X. M. Lv, B. W. Liu, H. Long, Y. D. Yang, J. L. Xiao, and Y. Du, "Modulation characteristics and microwave generation for AlGaInAs/InP microring lasers under four-wave mixing," Photon. Res. **2**, 177–181 (2014).
32. Y. D. Yang, J. L. Xiao, B. W. Liu, and Y. Z. Huang, "Mode characteristics and vertical radiation loss for AlGaInAs/InP microcylinder lasers," J. Opt. Soc. Am. B **32**, 439–444 (2015).
33. Y. D. Yang, H. Z. Weng, B. W. Liu, J. L. Xiao, and Y. Z. Huang, "Localized-cavity-loss-induced external mode coupling in optical microresonators," J. Opt. Soc. Am. B **32**, 2376–2381 (2015).
34. S. S. Sui, M. Y. Tang, Y. D. Yang, J. L. Xiao, Y. Du, and Y. Z. Huang, "Investigation of hybrid microring lasers adhesively bonded on silicon wafer," Photon. Res. **3**, 289–295 (2015).
35. S. Longhi and L. Feng, "Unidirectional lasing in semiconductor microring lasers at an exceptional point," Photon. Res. **5**, B1–B6 (2017).
36. X. C. Chen, C. S. Fenrich, M. Y. Xue, M. Y. Kao, K. Zang, C. Y. Lu, E. T. Fei, Y. S. Chen, Y. J. Huo, T. I. Kamins, and J. S. Harris, "Tensile-strained Ge/SiGe multiple quantum well microdisks," Photon. Res. **5**, B7–B14 (2017).
37. J. Y. Ma, X. S. Jiang, and M. Xiao, "Kerr frequency combs in large-size, ultra-high-Q toroid microcavities with low repetition rates," Photon. Res. **5**, B54–B58 (2017).
38. J. U. Nockel, A. D. Stone, G. Chen, H. L. Grossman, and R. K. Chang, "Directional emission from asymmetric resonant cavities," Opt. Lett. **21**, 1609–1611 (1996).
39. J. U. Nockel and A. D. Stone, "Ray and wave chaos in asymmetric resonant optical cavities," Nature **385**, 45–47 (1997).
40. C. Gmachl, F. Capasso, E. E. Narimanov, J. U. Nockel, A. D. Stone, J. Faist, D. L. Sivco, and A. Y. Cho, "High-power directional emission from microlasers with chaotic resonators," Science **280**, 1556–1564 (1998).
41. Y. Baryshnikov, P. Heider, W. Parz, and V. Zharnitsky, "Whispering gallery modes inside asymmetric resonant cavities," Phys. Rev. Lett. **93**, 133902 (2004).
42. S. K. Kim, S. H. Kim, G. H. Kim, H. G. Park, D. J. Shin, and Y. H. Lee, "Highly directional emission from few-micron-size elliptical microdisks," Appl. Phys. Lett. **84**, 861–863 (2004).

43. X. F. Jiang, Y. F. Xiao, Q. F. Yang, L. B. Shao, W. R. Clements, and Q. H. Gong, "Free-space coupled, ultralow-threshold Raman lasing from a silica microcavity," Appl. Phys. Lett. **103**, 101102 (2013).
44. Z. P. Liu, X. F. Jiang, Y. Li, Y. F. Xiao, L. Wang, J. L. Ren, S. J. Zhang, H. Yang, and Q. H. Gong, "High-*Q* asymmetric polymer microcavities directly fabricated by two-photon polymerization," Appl. Phys. Lett. **102**, 221108 (2013).
45. L. B. Shao, L. Wang, W. J. Xiong, X. F. Jiang, Q. F. Yang, and Y. F. Xiao, "Ultrahigh-*Q*, largely deformed microcavities coupled by a free-space laser beam," Appl. Phys. Lett. **103**, 121102 (2013).
46. L. Wang, D. Lippolis, Z. Y. Li, X. F. Jiang, Q. H. Gong, and Y. F. Xiao, "Statistics of chaotic resonances in an optical microcavity," Phys. Rev. E **93**, 040201 (2016).
47. J. W. Wang, Y. Yin, Q. Hao, S. Z. Huang, E. S. G. Naz, O. G. Schmidt, and L. B. Ma, "External strain enabled post-modification of nanomembrane-based optical microtube cavities," ACS Photon. **5**, 2060–2067 (2018).
48. J. W. Wang, Y. Yin, Q. Hao, Y. D. Yang, S. Valligatla, E. S. G. Naz, Y. Li, C. N. Saggau, L. B. Ma, and O. G. Schmidt, "Curved nanomembrane-based concentric ring cavities for supermode hybridization," Nano Lett. **18**, 7261–7267 (2018).
49. G. D. Chern, H. E. Tureci, A. D. Stone, R. K. Chang, M. Kneissl, and N. M. Johnson, "Unidirectional lasing from InGaN multiple-quantum-well spiral-shaped micropillars," Appl. Phys. Lett. **83**, 1710–1712 (2003).
50. C. M. Kim, J. Cho, J. Lee, S. Rim, S. H. Lee, K. R. Oh, and J. H. Kim, "Continuous wave operation of a spiral-shaped microcavity laser," Appl. Phys. Lett. **92**, 131110 (2008).
51. J. Wiersig and M. Hentschel, "Combining directional light output and ultralow loss in deformed microdisks," Phys. Rev. Lett. **100**, 033901 (2008).
52. Q. H. Song, W. Fang, B. Y. Liu, S. T. Ho, G. S. Solomon, and H. Cao, "Chaotic microcavity laser with high quality factor and unidirectional output," Phys. Rev. A **80**, 041807 (2009).
53. Q. H. Song, L. Ge, A. D. Stone, H. Cao, J. Wiersig, J. B. Shim, J. Unterhinninghofen, W. Fang, and G. S. Solomon, "Directional laser emission from a wavelength-scale chaotic microcavity," Phys. Rev. Lett. **105**, 130902 (2010).
54. X. F. Jiang, Y. F. Xiao, C. L. Zou, L. N. He, C. H. Dong, B. B. Li, Y. Li, F. W. Sun, L. Yang, and Q. H. Gong, "Highly unidirectional emission and ultralow-threshold lasing from on-chip ultrahigh-*Q* microcavities," Adv. Mater. **24**, OP260–OP264 (2012).
55. Y. D. Yang, Y. Zhang, Y. Z. Huang, and A. W. Poon, "Direct-modulated waveguide-coupled microspiral disk lasers with spatially selective injection for on-chip optical interconnects," Opt. Express **22**, 824–838 (2014).
56. Y. F. Xiao, X. F. Jiang, Q. F. Yang, L. Wang, K. B. Shi, Y. Li, and Q. H. Gong, "Tunneling-induced transparency in a chaotic microcavity," Laser Photon. Rev. **7**, L51–L54 (2013).
57. Q. F. Yang, X. F. Jiang, Y. L. Cui, L. B. Shao, and Y. F. Xiao, "Dynamical tunneling-assisted coupling of high-*Q* deformed microcavities using a free-space beam," Phys. Rev. A **88**, 023810 (2013).
58. Y. C. Liu, Y. F. Xiao, X. F. Jiang, B. B. Li, Y. Li, and Q. H. Gong, "Cavity-QED treatment of scattering-induced free-space excitation and collection in high-*Q* whispering-gallery microcavities," Phys. Rev. A **85**, 013843 (2012).
59. F. J. Shu, X. F. Jiang, G. M. Zhao, and L. Yang, "A scatterer-assisted whispering-gallery-mode microprobe," Nanophotonics **7**, 1455–1460 (2018).
60. H. C. Chang, G. Kioseoglou, E. H. Lee, J. Haetty, M. H. Na, Y. Xuan, H. Luo, A. Petrou, and A. N. Cartwright, "Lasing modes in equilateral-triangular laser cavities," Phys. Rev. A **62**, 013813 (2000).
61. Y. Z. Huang, W. H. Guo, and Q. M. Wang, "Influence of output waveguide on mode quality factor in semiconductor microlasers with an equilateral triangle resonator," Appl. Phys. Lett. **77**, 3511–3513 (2000).
62. A. W. Poon, F. Courvoisier, and R. K. Chang, "Multimode resonances in square-shaped optical microcavities," Opt. Lett. **26**, 632–634 (2001).
63. J. Wiersig, "Hexagonal dielectric resonators and microcrystal lasers," Phys. Rev. A **67**, 023807 (2003).
64. T. Nobis, E. M. Kaidashev, A. Rahm, M. Lorenz, and M. Grundmann, "Whispering gallery modes in nanosized dielectric resonators with hexagonal cross section," Phys. Rev. Lett. **93**, 103903 (2004).
65. N. Ma, C. Li, and A. W. Poon, "Laterally coupled hexagonal micropillar resonator add–drop filters in silicon nitride," IEEE Photon. Technol. Lett. **16**, 2487–2489 (2004).
66. S. V. Boriskina, T. M. Benson, P. Sewell, and A. I. Nosich, "Optical modes in 2-D imperfect square and triangular microcavities," IEEE J. Quantum Electron. **41**, 857–862 (2005).
67. G. M. Wysin, "Electromagnetic modes in dielectric equilateral triangle resonators," J. Opt. Soc. Am. B **23**, 1586–1599 (2006).
68. Y. D. Yang, Y. Z. Huang, and S. J. Wang, "Mode analysis for equilateral-triangle-resonator microlasers with metal confinement layers," IEEE J. Quantum Electron. **45**, 1529–1536 (2009).
69. C. X. Xu, J. Dai, G. P. Zhu, G. Y. Zhu, Y. Lin, J. T. Li, and Z. L. Shi, "Whispering-gallery mode lasing in ZnO microcavities," Laser Photon. Rev. **8**, 469–494 (2014).
70. Y. D. Yang and Y. Z. Huang, "Mode characteristics and directional emission for square microcavity lasers," J. Phys. D **49**, 253001 (2016).
71. H. Z. Weng, Y. D. Yang, J. L. Xiao, Y. Z. Hao, and Y. Z. Huang, "Spectral engineering for circular-side square microlasers," Opt. Express **26**, 9409–9414 (2018).
72. F. L. Wang, Y. D. Yang, Y. Z. Huang, Z. X. Xiao, and J. L. Xiao, "Single-transverse-mode waveguide-coupled deformed hexagonal resonator microlasers," Appl. Opt. **57**, 7242–7248 (2018).
73. Y. D. Yang and Y. Z. Huang, "Symmetry analysis and numerical simulation of mode characteristics for equilateral-polygonal optical microresonators," Phys. Rev. A **76**, 023822 (2007).
74. P. J. Richens and M. V. Berry, "Pseudointegrable systems in classical and quantum-mechanics," Physica D **2**, 495–512 (1981).
75. M. Tang, Y. D. Yang, H. Z. Weng, J. L. Xiao, and Y. Z. Huang, "Ray dynamics and wave chaos in circular-side polygonal microcavities," Phys. Rev. A **99**, 033814 (2019).
76. M. Lebental, N. Djellali, C. Arnaud, J. S. Lauret, J. Zyss, R. Dubertrand, C. Schmit, and E. Bogomolny, "Inferring periodic orbits from spectra of simply shaped microlasers," Phys. Rev. A **76**, 023830 (2007).
77. M. H. Huang, S. Mao, H. Feick, H. Q. Yan, Y. Y. Wu, H. Kind, E. Weber, R. Russo, and P. D. Yang, "Room-temperature ultraviolet nanowire nanolasers," Science **292**, 1897–1899 (2001).
78. C. Kim, Y. J. Kim, E. S. Jang, G. C. Yi, and H. H. Kim, "Whispering-gallery-mode like-enhanced emission from ZnO nanodisk," Appl. Phys. Lett. **88**, 093104 (2006).
79. C. Czekalla, C. Sturm, R. Schmidt-Grund, B. Q. Cao, M. Lorenz, and M. Grundmann, "Whispering gallery mode lasing in zinc oxide microwires," Appl. Phys. Lett. **92**, 241102 (2008).
80. D. J. Gargas, M. C. Moore, A. Ni, S. W. Chang, Z. Y. Zhang, S. L. Chuang, and P. D. Yang, "Whispering gallery mode lasing from zinc oxide hexagonal nanodisks," ACS Nano **4**, 3270–3276 (2010).
81. C. Tessarek, G. Sarau, M. Kiometzis, and S. Christiansen, "High quality factor whispering gallery modes from self-assembled hexagonal GaN rods grown by metal-organic vapor phase epitaxy," Opt. Express **21**, 2733–2740 (2013).
82. C. Tessarek, R. Roder, T. Michalsky, S. Geburt, H. Franke, R. Schmidt-Grund, M. Heilmann, B. Hoffmann, C. Ronning, M. Grundmann, and S. Christiansen, "Improving the optical properties of self-catalyzed GaN microrods toward whispering gallery mode lasing," ACS Photon. **1**, 990–997 (2014).
83. D. Wang, H. W. Seo, C. C. Tin, M. J. Bozack, J. R. Williams, M. Park, and Y. Tzeng, "Lasing in whispering gallery mode in ZnO nanonails," J. Appl. Phys. **99**, 093112 (2006).
84. J. Dai, C. X. Xu, K. Zheng, C. G. Lv, and Y. P. Cui, "Whispering gallery-mode lasing in ZnO microrods at room temperature," Appl. Phys. Lett. **95**, 241110 (2009).
85. G. P. Zhu, C. X. Xu, J. Zhu, C. G. Lv, and Y. P. Cui, "Two-photon excited whispering-gallery mode ultraviolet laser from an individual ZnO microneedle," Appl. Phys. Lett. **94**, 051106 (2009).
86. R. Chen, B. Ling, X. W. Sun, and H. D. Sun, "Room temperature excitonic whispering gallery mode lasing from high-quality hexagonal ZnO microdisks," Adv. Mater. **23**, 2199–2204 (2011).

87. T. Kouno, K. Kishino, and M. Sakai, "Lasing action on whispering gallery mode of self-organized GaN hexagonal microdisk crystal fabricated by RF-plasma-assisted molecular beam epitaxy," IEEE J. Quantum Electron. **47**, 1565–1570 (2011).
88. S. J. Wang, Y. D. Yang, and Y. Z. Huang, "Analysis of mode characteristics for equilateral-polygonal resonators with a center hole," J. Opt. Soc. Am. B **26**, 2449–2454 (2009).
89. J. D. Lin, Y. Z. Huang, Y. D. Yang, Q. F. Yao, X. M. Lv, J. L. Xiao, and Y. Du, "Single transverse whispering-gallery mode AlGaInAs/InP hexagonal resonator microlasers," IEEE Photon. J. **3**, 756–764 (2011).
90. H. H. Fang, R. Ding, S. Y. Lu, Y. D. Yang, Q. D. Chen, J. Feng, Y. Z. Huang, and H. B. Sun, "Whispering-gallery mode lasing from patterned molecular single-crystalline microcavity array," Laser Photon. Rev. **7**, 281–288 (2013).
91. Z. X. Xiao, Y. Z. Huang, Y. D. Yang, J. L. Xiao, and X. W. Ma, "Single-mode unidirectional-emission circular-side hexagonal resonator microlasers," Opt. Lett. **42**, 1309–1312 (2017).
92. Y. D. Yang, H. Z. Weng, Y. Z. Hao, J. L. Xiao, and Y. Z. Huang, "Square microcavity semiconductor lasers," Chin. Phys. B **27**, 114212 (2018).
93. T. Akasaka, Y. Kobayashi, S. Ando, and N. Kobayashi, "GaN hexagonal microprisms with smooth vertical facets fabricated by selective metalorganic vapor phase epitaxy," Appl. Phys. Lett. **71**, 2196–2198 (1997).
94. Q. H. Song, L. Ge, J. Wiersig, and H. Cao, "Formation of long-lived resonances in hexagonal cavities by strong coupling of superscar modes," Phys. Rev. A **88**, 023834 (2013).
95. T. Kouno, M. Sakai, K. Kishino, and K. Hara, "Optical microresonant modes acting in thin hexagonal GaN microdisk," Jpn. J. Appl. Phys. **53**, 072001 (2014).
96. Z. Y. Gu, K. Y. Wang, W. Z. Sun, S. Liu, N. Zhang, S. M. Xiao, and Q. H. Song, "Triangular lasing modes in hexagonal perovskite microplates with balanced gain and loss," RSC Adv. **6**, 64589–64594 (2016).
97. Y. Z. Huang, Q. Chen, W. H. Guo, Q. Y. Lu, and L. J. Yu, "Mode characteristics for equilateral triangle optical resonators," IEEE J. Sel. Top. Quantum Electron. **12**, 59–65 (2006).
98. J. Wiersig, "Formation of long-lived, scarlike modes near avoided resonance crossings in optical microcavities," Phys. Rev. Lett. **97**, 253901 (2006).
99. Y. D. Yang and Y. Z. Huang, "Mode analysis and Q-factor enhancement due to mode coupling in rectangular resonators," IEEE J. Quantum Electron. **43**, 497–502 (2007).
100. T. Nobis and M. Grundmann, "Low-order optical whispering-gallery modes in hexagonal nanocavities," Phys. Rev. A **72**, 063806 (2005).
101. S. Ando, N. Kobayashi, and H. Ando, "Novel hexagonal-facet GaAs/AlGaAs laser grown by selective-area metalorganic chemical-vapor-deposition," Jpn. J. Appl. Phys. **32**, L1293–L1296 (1993).
102. U. Vietze, O. Krauss, F. Laeri, G. Ihlein, F. Schuth, B. Limburg, and M. Abraham, "Zeolite-dye microlasers," Phys. Rev. Lett. **81**, 4628–4631 (1998).
103. I. Braun, G. Ihlein, F. Laeri, J. U. Nockel, G. Schulz-Ekloff, F. Schuth, U. Vietze, and O. Weiss, "Hexagonal microlasers based on organic dyes in nanoporous crystals," Appl. Phys. B **70**, 335–343 (2000).
104. H. J. He, E. Ma, Y. J. Cui, J. C. Yu, Y. Yang, T. Song, C. D. Wu, X. Y. Chen, B. L. Chen, and G. D. Qian, "Polarized three-photon-pumped laser in a single MOF microcrystal," Nat. Commun. **7**, 11087 (2016).
105. R. Medishetty, J. K. Zareba, D. Mayer, M. Samoc, and R. A. Fischer, "Nonlinear optical properties, upconversion and lasing in metal-organic frameworks," Chem. Soc. Rev. **46**, 4976–5004 (2017).
106. Q. Zhang, S. T. Ha, X. F. Liu, T. C. Sum, and Q. H. Xiong, "Room-temperature near-infrared high-Q perovskite whispering-gallery planar nano lasers," Nano Lett. **14**, 5995–6001 (2014).
107. X. F. Liu, S. T. Ha, Q. Zhang, M. de la Mata, C. Magen, J. Arbiol, T. C. Sum, and Q. H. Xiong, "Whispering gallery mode lasing from hexagonal shaped layered lead iodide crystals," ACS Nano **9**, 687–695 (2015).
108. J. Dai, C. X. Xu, and X. W. Sun, "ZnO-microrod/p-GaN heterostructured whispering-gallery-mode microlaser diodes," Adv. Mater. **23**, 4115–4119 (2011).
109. G. Y. Zhu, C. X. Xu, Y. Lin, Z. L. Shi, J. T. Li, T. Ding, Z. S. Tian, and G. F. Chen, "Ultraviolet electroluminescence from horizontal ZnO microrods/GaN heterojunction light-emitting diode array," Appl. Phys. Lett. **101**, 041110 (2012).
110. G. Y. Zhu, J. T. Li, Z. S. Tian, J. Dai, Y. Y. Wang, P. L. Li, and C. X. Xu, "Electro-pumped whispering gallery mode ZnO microlaser array," Appl. Phys. Lett. **106**, 021111 (2015).
111. Y. Y. Wang, C. X. Xu, M. M. Jiang, J. T. Li, J. Dai, J. F. Lu, and P. L. Li, "Lasing mode regulation and single-mode realization in ZnO whispering gallery microcavities by the Vernier effect," Nanoscale **8**, 16631–16639 (2016).
112. Q. X. Zhu, F. F. Qin, J. F. Lu, Z. Zhu, H. Y. Nan, Z. L. Shi, Z. H. Ni, and C. X. Xu, "Synergistic graphene/aluminum surface plasmon coupling for zinc oxide lasing improvement," Nano Res. **10**, 1996–2004 (2017).
113. C. X. Xu, F. F. Qin, Q. X. Zhu, J. F. Lu, Y. Y. Wang, J. T. Li, Y. Lin, Q. N. Cui, Z. L. Shi, and A. G. Manohari, "Plasmon-enhanced ZnO whispering-gallery mode lasing," Nano Res. **11**, 3050–3064 (2018).
114. J. Dai, C. X. Xu, X. W. Sun, and X. H. Zhang, "Exciton–polariton microphotoluminescence and lasing from ZnO whispering-gallery mode microcavities," Appl. Phys. Lett. **98**, 161110 (2011).
115. Q. Q. Duan, D. Xu, W. H. Liu, J. Lu, L. Zhang, J. Wang, Y. L. Wang, J. Gu, T. Hu, W. Xie, X. C. Shen, and Z. H. Chen, "Polariton lasing of quasi-whispering gallery modes in a ZnO microwire," Appl. Phys. Lett. **103**, 022103 (2013).
116. Y. Y. Lai, Y. P. Lan, and T. C. Lu, "Strong light–matter interaction in ZnO microcavities," Light: Sci. Appl. **2**, e76 (2013).
117. Y. Y. Lai, Y. H. Chou, Y. P. Lan, T. C. Lu, S. C. Wang, and Y. Yamamoto, "Crossover from polariton lasing to exciton lasing in a strongly coupled ZnO microcavity," Sci. Rep. **6**, 20581 (2016).
118. L. K. van Vugt, S. Ruhle, P. Ravindran, H. C. Gerritsen, L. Kuipers, and D. Vanmaekelbergh, "Exciton polaritons confined in a ZnO nanowire cavity," Phys. Rev. Lett. **97**, 147401 (2006).
119. L. X. Sun, Z. H. Chen, Q. J. Ren, K. Yu, L. H. Bai, W. H. Zhou, H. Xiong, Z. Q. Zhu, and X. C. Shen, "Direct observation of whispering gallery mode polaritons and their dispersion in a ZnO tapered microcavity," Phys. Rev. Lett. **100**, 156403 (2008).
120. A. Trichet, L. Sun, G. Pavlovic, N. A. Gippius, G. Malpuech, W. Xie, Z. Chen, M. Richard, and L. Dang, "One-dimensional ZnO exciton polaritons with negligible thermal broadening at room temperature," Phys. Rev. B **83**, 041302 (2011).
121. W. Xie, H. X. Dong, S. F. Zhang, L. X. Sun, W. H. Zhou, Y. J. Ling, J. Lu, X. C. Shen, and Z. H. Chen, "Room-temperature polariton parametric scattering driven by a one-dimensional polariton condensate," Phys. Rev. Lett. **108**, 166401 (2012).
122. D. Xu, W. Xie, W. H. Liu, J. Wang, L. Zhang, Y. L. Wang, S. F. Zhang, L. X. Sun, X. C. Shen, and Z. H. Chen, "Polariton lasing in a ZnO microwire above 450 K," Appl. Phys. Lett. **104**, 082101 (2014).
123. S. F. Li and A. Waag, "GaN based nanorods for solid state lighting," J. Appl. Phys. **111**, 071101 (2012).
124. C. Tessarek, M. Heilmann, and S. Christiansen, "Whispering gallery modes in GaN microdisks, microrods and nanorods grown by MOVPE," Phys. Status Solidi C **11**, 794–797 (2014).
125. H. Baek, J. K. Hyun, K. Chung, H. Oh, and G. C. Yi, "Selective excitation of Fabry–Perot or whispering-gallery mode-type lasing in GaN microrods," Appl. Phys. Lett. **105**, 201108 (2014).
126. Y. Y. Zhang, X. H. Zhang, K. H. Li, Y. F. Cheung, C. Feng, and H. W. Choi, "Advances in III-nitride semiconductor microdisk lasers," Phys. Status Solidi A **212**, 960–973 (2015).
127. M. Moewe, L. C. Chuang, S. Crankshaw, K. W. Ng, and C. Chang-Hasnain, "Core–shell InGaAs/GaAs quantum well nanoneedles grown on silicon with silicon-transparent emission," Opt. Express **17**, 7831–7836 (2009).
128. R. Chen, T. T. D. Tran, K. W. Ng, W. S. Ko, L. C. Chuang, F. G. Sedgwick, and C. Chang-Hasnain, "Nanolasers grown on silicon," Nat. Photonics **5**, 170–175 (2011).
129. T. Kouno, S. Suzuki, K. Kishino, M. Sakai, K. Yamano, A. Yanagihara, and K. Hara, "Optical properties of arrays of hexagonal GaN microdisks acting as whispering-gallery-mode-type optical microcavities," Phys. Status Solidi A **212**, 1017–1020 (2015).

130. Y. D. Yang, S. J. Wang, and Y. Z. Huang, "Investigation of mode coupling in a microdisk resonator for realizing directional emission," Opt. Express **17**, 23010–23015 (2009).
131. Q. H. Song, L. Ge, B. Redding, and H. Cao, "Channeling chaotic rays into waveguides for efficient collection of microcavity emission," Phys. Rev. Lett. **108**, 243902 (2012).
132. H. Z. Weng, Y. Z. Huang, Y. D. Yang, X. W. Ma, J. L. Xiao, and Y. Du, "Mode *Q* factor and lasing spectrum controls for deformed square resonator microlasers with circular sides," Phys. Rev. A **95**, 013833 (2017).
133. M. Tang, Y. Z. Huang, Y. D. Yang, H. Z. Weng, and Z. X. Xiao, "Variable-curvature microresonators for dual-wavelength lasing," Photon. Res. **5**, 695–701 (2017).
134. H. Long, Y. Z. Huang, X. W. Ma, Y. D. Yang, J. L. Xiao, L. X. Zou, and B. W. Liu, "Dual-transverse-mode microsquare lasers with tunable wavelength interval," Opt. Lett. **40**, 3548–3551 (2015).
135. J. L. Xiao, C. G. Ma, Z. X. Xiao, Y. D. Yang, and Y. Z. Huang, "Random bit generation in dual transverse mode microlaser without optical injection or feedback," in *IEEE International Semiconductor Laser Conference ISLC* (2018), pp. 171–172.